The Journal of Chemical Physics

RESEARCH ARTICLE | AUGUST 22 2024

Mie scattering theory applied to light scattering of large nonhomogeneous colloidal spheres

Christian Balderas-Cabrera ; Rolando Castillo

J. Chem. Phys. 161, 084903 (2024)
https://doi.org/10.1063/5.0216489

The Journal of Chemical Physics ARTICLE pubs.aip.org/aip/jcp

Mie scattering theory applied to light scattering of large nonhomogeneous colloidal spheres

Cite as: J. Chem. Phys. 161, 084903 (2024); doi: 10.1063/5.0216489
Submitted: 29 April 2024 • Accepted: 7 August 2024 •
Published Online: 22 August 2024

Christian Balderas-Cabrera and Rolando Castillo[a)]

AFFILIATIONS

Instituto de Física, Universidad Nacional Autónoma de México, P.O. Box 20-364, 01000 Mexico City, Mexico

[a)]Author to whom correspondence should be addressed: rolandoc@fisica.unam.mx

ABSTRACT

Colloidal suspensions made of smart core–shell structures are of current interest in many fields. Their properties come from the possibility of varying the core and shell materials for modifying the composite particles' chemical, biological, and optical properties. These particles are formed with a material with a constant refractive index core and a shell with a refractive index decaying until it matches the solvent refractive index. Poly(N-IsoPropyl AcrylaMide) (PNIPAM) is a typical example of materials forming shells. In this report, we present how to apply Mie scattering theory to predict and understand the static light scattering of large nonhomogeneous colloidal particles with spherical symmetry whose size is comparable with or larger than the light wavelength used for developing scattering experiments, where the Rayleigh–Gans–Debye approximation is not valid. Here, the refractive index decay was approximated by a Gaussian RI profile numerically evaluated through a multilayer sphere. We calculated the form factor functions of suspensions of PNIPAM microgels previously reported and core–shell suspensions made of polystyrene/PNIPAM at 20 and 40 °C synthesized by us. In all the cases, our method succeeded in providing the scattering intensity as a function of the angle. The software for using the numerical method is fairly straightforward and is accessible as an open-source code. The results can not only help predict and understand the photonic properties of microgels with large core–shell structures but also for any particle with a refractive index distribution with spherical symmetry, as in the case of microgels with super chaotropic agents, hollow microgels, or microparticles.

I. INTRODUCTION

The visible appearance of colloidal suspensions strongly depends on how they scatter light, which depends on the colloidal particle sizes and the ratio of refractive indexes between particles and the solvent where they are embedded. However, colloidal particles can be quite complex nowadays, as shown by colloidal suspensions made of core–shell structures. Core–shell particles are made of two or more material layers. One forms the inner core, and the others make the outer layers or the shell. This design allows tuning these composite materials to exhibit characteristics and properties that are not achievable by the individual core or shell materials. These have advantages and unique properties because adjusting the core and shell materials affects the composite particles' biological, chemical, magnetic, and optical properties that disclose multiple applications.[1–7] One example could be microgels, where polymer networks can be swollen by the solvent in which they are embedded. Their particle sizes (from tens of nanometers to several micrometers) and shapes (spherical, anisotropic, and hollow) can be controlled through synthetic design. Microgels seem to have an unlimited tunability employing countless responsive polymers, making them an unrestricted range of applications, including drug delivery systems biosensors,[1,2,8] actuators,[7,9] tissue engineering scaffolds,[8] and many more.[3–5,10]

Poly(N-IsoPropyl AcrylaMide) (PNIPAM) microgel suspensions are made of stimuli-sensitive gel particles obtained during cross-linking polymerization of NIPAM, which is thermosensitive because the tunable network changes their size with temperature.[11–13] PNIPAM in water forms particles with a constant refractive index core and a shell with a refractive index decaying until it matches the solvent refractive index, forming a core–shell structure.[14] When their suspensions are warmed above their cloud point, they undergo a reversible phase transition from a hydrated state (expanded particles) to a dehydrated state (shrunk particles). This transition presents an LCST that occurs around 32 °C depending on the polymer concentration, the molar mass of polymer chains, and polymer polydispersity; salts and organic compounds can alter the cloud point temperature.[11,14] The PNIPAM microgel particles

have a non-constant density mass profile and, consequently, a non-constant refractive index profile, generally described as a core–shell structure with an inner constant dense region and a fuzzy shell, where the density decreases approximately as a Gaussian function when the temperature is below the LCST.[14–17] Therefore, the PNIPAM microgel is an excellent candidate for a model system to get the scattering properties of core–shell systems, dynamically tunable, which is of current interest.[6,7,9,12,18–21] Since PNIPAM expels its liquid content at a temperature near the human body, PNIPAM copolymers are under research for possible applications in tissue engineering and controlled drug delivery.[2,8,22,23] In addition to the mentioned applications involving core–shell particles, they could provide quantitative information about the ergodic–nonergodic transition in systems with repulsive interactions, as in crystallization and the glass transition,[24–26] where understanding their scattering properties is desirable.

Scattering theory relates the effect of an inhomogeneous medium on an incident electromagnetic wave, and the direct scattering problem aims to determine the scattered field by knowing the incident one, the scatterer properties, and the equations governing the wave motion. In particular, when a light beam illuminates a particle, the amount and angular distribution of scattered light and the amount of absorbed light depend on the particle's nature, shape, size, and material composition. In this context, the Rayleigh–Gans–Debye (RGD) approximation is used to evaluate the scattering form factor in scattering experiments such as small-angle neutron scattering (SANS) or static light scattering (SLS). For example, the RGD fuzzy sphere model is used to determine the scattering properties of PNIPAM microgel suspensions, as presented by Stieger *et al.*,[15,27] where they evaluated the scattering form factor as the convolution of the sphere scattering form factor with a Gaussian function. Recently, Simons *et al.*[10] used the RGD multi-sphere approximation to evaluate the scattering form factor for PNIPAM microgels decorated with super chaotropic nano-ions, measured by using small-angle x-ray scattering, as the sum of spheres with different contrast densities.[10,28]

However, all RGD approximations are valid for light scattering only when particles are small compared to the wavelength of the incident laser radiation and have a slight refractive index difference from the surrounding solvent.[29] A scattering theory for a detailed description of the radiative properties of nonhomogeneous microgels when their size is comparable with or larger than the light wavelength is lacking,[17,27] which could be helpful to study a case of great relevance nowadays, microgels with ionic guest molecules bound on the microgel structure (super chaotropic agents),[10] which can change their network size to be larger than the light wavelength used to study them with light scattering, or in the case of hollow microgel particles of ultra-low cross-linked microgels that have an inverted density profile in contrast to conventional fuzzy microgels, which show significantly higher deformability and spreading at interfaces in comparison with conventional PNIPAM microgels.[28] On the other hand, Mie scattering theory provides a general solution to Maxwell's equations in linear media, where it is only necessary to know the geometrical parameters and the dielectric properties of the scattering particles and the media where they are embedded to evaluate their radiative properties. It has the advantage of describing the light scattered from mesoscopic particles, which have a size comparable with or larger than the wavelength of light scattering off the particles. Mie scattering theory can also determine the scattering properties for multilayered spheres.[30] If the material has continuous radial nonhomogeneous dielectric properties, multilayer Mie scattering theory can also determine the scattering properties if some appropriate approximation to handle the inhomogeneity is employed. This kind of approximation has been tested successfully with the Luneburg lens.[30–32] The PNIPAM microgel radiative properties, which present a continuous radial nonhomogeneous RI index profile, can be approximated as a multilayer scattering sphere, as shown in the following. Recently, a multilayer Mie approximation has been applied for describing the extinction of PNIPAM core–shell with metallic cores in the visible spectrum, where RGD provides an excellent description of a form factor measured with SANS; however, it does not adequately describe the radiative properties in the visible spectrum.[33]

The main goal of this paper is to present how to apply the Mie scattering theory to the light scattering of large nonhomogeneous colloidal particles with spherical symmetry of a size comparable with the light wavelength used for developing light scattering experiments. In many examples, these particles can be described as formed by a core and a fuzzy shell, as those present in PNIPAM microgel suspensions or those made of a hard core and PNIPAM shell. To show the potential of our method, we present numerical calculations for core–shell particles of various sizes, cores with different refractive indices or hollow particles. Our results are also compared to the experimental data reported in the literature for PNIPAM microgels and with scattering experimental results for core–shell particles that we prepared (polystyrene/PNIPAM). Our method successfully gives the scattering intensity as a function of the angle. The method developed here could be used for studying microgels when super chaotropic agents are bound to the microgel structure[10] or hollow microgel particles.[5,34]

II. THEORETICAL MODEL AND NUMERICAL METHODS

A. Mie scattering for a multilayered sphere

The Mie scattering model solves Maxwell's equations for a monochromatic plane wave with wavelength λ propagating in a medium with refractive index (RI) n_0 scattered by a sphere with linear properties, radius R, and RI = n_p.[35] The differential scattering cross section in the far field, $d\sigma/d\Omega = F(\theta)$, provides the angular behavior of the light scattered by the sphere, where $F(\theta)$ is also known as the form factor function. Following the treatment of Bohren and Huffman,[35] the form factor function is given by

$$F(\theta) = \frac{1}{2}\left(|S_1(\theta)|^2 + |S_2(\theta)|^2\right), \tag{1}$$

where $S_1(\theta)$ and $S_2(\theta)$ are the amplitude scattering coefficients given by

$$S_1(\theta) = \sum_n \frac{2n+1}{n(n+1)}\left(a_n\pi_n(\theta) + b_n\tau_n(\theta)\right), \tag{2}$$

$$S_2(\theta) = \sum_n \frac{2n+1}{n(n+1)}\left(a_n\tau_n(\theta) + b_n\pi_n(\theta)\right), \tag{3}$$

where $\pi_n(\theta)$ and $\tau_n(\theta)$ are angular functions given by

$$\pi_n = \frac{P_n^1(\theta)}{\sin\theta}, \quad \tau = \frac{dP_n^1(\theta)}{d\theta}, \tag{4}$$

where $P_n^1(\theta)$ are the Legendre polynomials of degree n. In addition, in Eq. (3), a_n and b_n are the scattering coefficients determined by the boundary conditions between the medium and the sphere. They are related to the size parameter $x = 2\pi n_0 R/\lambda$ and the relative refractive index $m = n_p/n_0$.

Aden and Kerker[32,36] developed the generalization of the Mie Scattering model to a stratified sphere in L layers. They found that the functional form of $F(\theta)$, $S_1(\theta)$, and $S_2(\theta)$ are the same as in the Mie scattering by a single homogeneous sphere, given in Eqs. (1)–(3). Nevertheless, the scattering coefficients are now determined by the boundary conditions of the different interfaces and the outer layer with the medium; tangential components of the electric and magnetic fields $\boldsymbol{E}$ and $\boldsymbol{H}$ must be continuous across the boundaries. One of the most stable algorithms to efficiently find the scattering coefficients was developed by Yang,[30] who proposed to use Bessel functions of the first kind and Hankel functions of the first kind to describe the scattered fields in the layers instead of the typical solution, which takes Bessel functions of the first and the second kind.[30,35] Following Yang's algorithm, for a multilayered sphere with L layers labeled from the inner layer or core sphere to the outer layer, where the l layer has a size parameter $x_l = 2\pi n_0 r_l/\lambda = k_0 r_l$ and a relative refractive index $m_l = n_l/n_0$ (see Fig. 1), the scattering coefficients at the interface between l and $l+1$ layer are determined recursively by

$$A_n^{l+1} = R_n(m_{l+1}x_l)\frac{m_{l+1}H_n^a(m_l x_l) - m_l D_n^{(1)}(m_{l+1}x_l)}{m_{l+1}H_n^a(m_l x_l) - m_l D_n^{(3)}(m_{l+1}x_l)}, \tag{5}$$

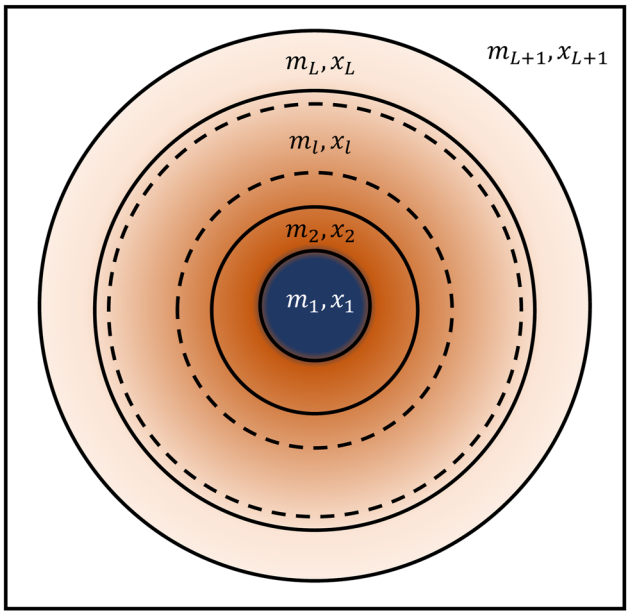

FIG. 1. Sketch of the geometry of a multilayered sphere labeled from the inner to the outer sphere. The intensity of color corresponds to the density.

$$B_n^{l+1} = R_n(m_{l+1}x_l)\frac{m_l H_n^b(m_l x_l) - m_{l+1} D_n^{(1)}(m_{l+1}x_l)}{m_l H_n^b(m_l x_l) - m_{l+1} D_n^{(3)}(m_{l+1}x_l)}, \tag{6}$$

where $H_n^a(z)$ and $H_n^b(z)$ are given by

$$H_n^a(m_l x_l) = \frac{R_n(m_l x_l)D_n^{(1)}(m_l x_l) - A_n^l D_n^{(3)}(m_l x_l)}{R_n(m_l x_l) - A_n^l}, \tag{7}$$

$$H_n^b(m_l x_l) = \frac{R_n(m_l x_l)D_n^{(1)}(m_l x_l) - B_n^l D_n^{(3)}(m_l x_l)}{R_n(m_l x_l) - B_n^l}, \tag{8}$$

beginning at $l = 1$, where $A_n^1 = B_n^1 = 0$. Here, $D_n^{(1)}(z) = \psi_n'(z)/\psi_n(z)$ and $D_n^{(3)}(z) = \zeta_n'(z)/\zeta(z)$ are the logarithmical derivative of the Bessel function of the first kind $\psi_n(z)$ and the Hankel function of the first kind $\zeta_n(z)$, respectively, and $R_n(z) = \psi_n(z)/\zeta_n(z)$. The recursion algorithm finishes at $l = L+1$, i.e., in the outer region of the sphere where the scattering coefficients, a_n and b_n, are given by

$$a_n = A_n^{L+1} = \frac{[H_n^a(m_L x_L)/m_L + n/x_L]\psi_n(x_L) - \psi_{n-1}(x_L)}{[H_n^a(m_L x_L)/m_L + n/x_L]\zeta_n(x_L) - \zeta_{n-1}(x_L)}, \tag{9}$$

$$b_n = B_n^{L+1} = \frac{[m_L H_n^b(m_L x_L)/m_L + n/x_L]\psi_n(x_L) - \psi_{n-1}(x_L)}{[m_L H_n^b(m_L x_L)/m_L + n/x_L]\zeta_n(x_L) - \zeta_{n-1}(x_L)}. \tag{10}$$

After computing the scattering coefficients a_n and b_n in Eqs. (9) and (10), the multilayered sphere's radiative properties can be evaluated.[30,35] In an unpolarized light scattering experiment, the angular scattering intensity by a particle is $I(\theta) \propto F(\theta)$, and in a vertical–vertical polarized light, scattering by a particle is $I_\perp(\theta) \propto |S_1(\theta)|^2$.[35]

Yang's algorithm was coded in Fortran and compiled with the GNU Fortran compiler. We replicate the form factor of the Luneburg lens to test our algorithm.[30–32] The Luneburg lens has a continuum refractive index function given by $m(r) = \sqrt{2-(r/a)^2}$, with

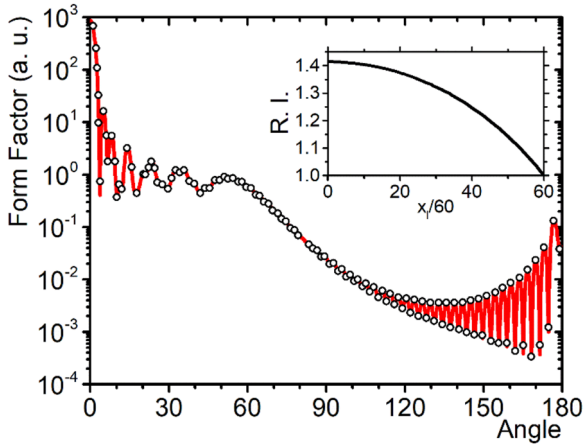

FIG. 2. Form factor function as a function of scattering angle (degrees) for a Luneburg lens with the external size parameter $x_L = 60$ and discretized with 500 layers. Inset: the relative refractive index as a function of the size parameter of the sphere layers. The circles were digitalized from a continuous curve from Refs. 30 and 31.

a being the radius of the sphere, which could be approximated as a multilayered sphere. In Fig. 2, we show the form factor function for a Luneburg lens with a size parameter $x_L = 60$ and $L = 500$ equidistant layers with relative refractive index $m(\bar{x}_l) = \sqrt{2 - (\bar{x}_l/x_a)^2}$, where $\bar{x}_l = (x_{l-1} + x_l)/2$ and $x_a = k_0 a$. In the inset of Fig. 2, the refractive index profile is shown. Our results are consistent with the others reported in the literature.[30,31]

B. Radial refractive index profile for microgels of PNIPAM

PNIPAM microgels have a non-constant density mass profile, generally described as a core–shell structure with an inner constant dense region, also known as the core, and a fuzzy shell, where the density decreases approximately as a Gaussian function.[14–17] Some authors suggest that in PNIPAM microgels, the RI is proportional to its density profile, and the shell RI profile could be modeled as[16]

$$n(r) = (n_c - n_0)\exp\left(-\frac{1}{2}\frac{(r-R_c)^2}{\sigma^2}\right) + n_0, \quad R_c < r \le R_s, \qquad (11)$$

with R_c being the core radius with a constant RI, R_s is the shell radius, and n_c and n_0 are the core and solvent refractive indexes, respectively. To use the multilayer sphere approximation, we discretize this RI profile with the first layer, $l = 1$, with $x_1 = k_0 R_c$ and $m_1 = n_c/n_0$, and successive $L - 1$ equally spaced layers with $m_l = n(\bar{x}_l)/n_0$, where $\bar{x}_l = (x_{l-1} + x_l)/2$ for $l = 2, \ldots, L$. In the last layer, $x_L = k_0 R_s$, the RI of PNIPAM, and the medium match. The relative RI of the last layer is defined arbitrarily as $m_L = (n_0 + 0.0001)/n_0$ by numerical convenience. Therefore, with the given R_c, R_s, n_c, and n_0, the value of σ can be calculated.

In the inset of Fig. 3, we show the RI profile for a mesoscopic core–shell sphere with $R_c = 290$ nm, $R_s = 437$ nm, $n_c = 1.45$, and $n_0 = 1.332$, discretized with three layers, 30 layers, and 500 layers. While the RI profile for 3 and 30 layers is a rough approximation, the RI profile for 500 layers approximation is almost a smooth curve. In Fig. 3, we present the form factors for the three cases, which are similar despite the roughness approximations with 3 and 30 layers. Notably, the form factors for the 30- and 500-layer approximation are essentially the same. Therefore, we will consider a 30-layer approximation to be an excellent approximation of the continuous case. In the following, in Sec. III C, we will go back to this issue.

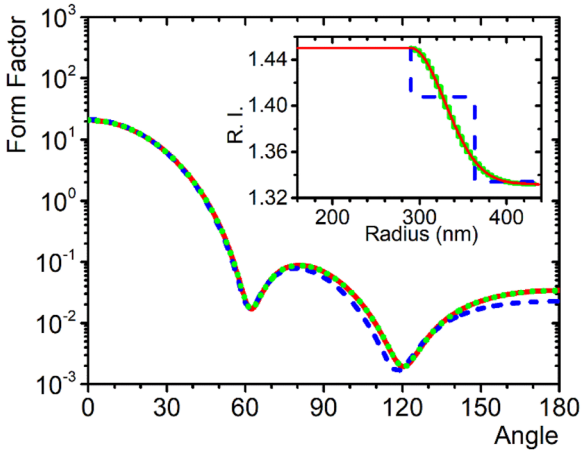

FIG. 3. Form factor functions (arbitrary units) for mesoscopic particles (Diam. $= 2R_s > \lambda$), vs angle (degrees) for the three radial refractive index profiles given in the inset. The core RI is the same in all the cases. Inset: radial refractive index profile model for a PNIPAM microgel approximated as a multilayer sphere with three layers (dashed blue line), 30 layers (dotted black line), and 500 layers (solid red line).

C. Polydispersity model

In a static light scattering experiment in the absence of multiple scattering, the total scattering intensity, $I_T(\theta)$ of a monodisperse system is $I_T(\theta) \propto NI(\theta)$, with N scatterers. However, the particles embedded in a fluid are rarely monodisperse, so the effect of scatterers' polydispersity must be considered. Polydispersity can be evaluated considering the scattering intensity average over radii with a size distribution $\rho(R)$. Then, the total scattering intensity for core–shell particles is[37,38]

$$I_T(\theta) \propto N\bar{I}(\theta) = N\int_{R_s}\int_{R_c} I(R_c, R_s, \theta)\rho(R_c)\rho(R_s)dR_c dR_s. \qquad (12)$$

Here, we consider polydispersity in the core, R_c, and shell, R_s. In our case, the particle size distribution will follow the log-normal distribution function in both cases; they are given by[38]

$$\rho(R) = \frac{\exp\left(-0.5[\ln\sigma_g]^2\right)}{2R\sqrt{2\pi}\ln(\sigma_g)}\exp\left\{-\frac{1}{2}\left[\frac{\ln(R) - \ln(\bar{R})}{\ln\sigma_g}\right]^2\right\}, \qquad (13)$$

where $\bar{R}$ is the mean radius and σ_g is the geometric standard deviation, which is a measure of polydispersity that must be greater than 1. If $\sigma_g = 1$, particles are monodisperse. For sampling most of the radii population, the integration limits are given by $R = \bar{R}\sigma_g^{\pm\sqrt{18}}$.[38] The numerical solution of the integral is performed by using the Gaussian–Legendre quadrature.

III. MATERIAL AND METHODS

A. Synthesis

We synthesized PS/PNIPAM core–shell particles following the reported protocol by Zhu *et al.*[34] We used polystyrene (PS) spheres with a mean diameter of 99 nm from a 10.02% w/w water suspension (Bangs Laboratories, Inc. USA) as seeds. They were cleaned by dialysis; water was exchanged for ethanol by centrifugation; and the suspension was dispersed by sonication. Reagents were used as received: N-IsoproPylAcrylaMide (NIPAM) (≥99%, Sigma-Aldrich, USA); N, N′-MethyleneBis(Acrylamide) (MBA) (99%, Sigma-Aldrich, USA); and AzobIsisoButyroNitrile [AIBN, 2,2′-Azobis(2-methylpropioNitrile)] (99%, Sigma-Aldrich, USA). The ethanol suspension of 0.2792 g of PS-cleaned seeds was mixed with 0.0315 g of AIBN initiator in 38 ml of ethanol and sonicated for 30 min. This suspension was added to a three-neck flask with N_2 atmosphere, mixed with 300 ml of degassed deionized water and constant stirring. Then, 2.136 g of NIPAM and 0.292 g of MBA were added to the solution suspension, which was heated to 76 °C for 4 h of polymerization. The reaction product is cooled at room temperature with constant stirring. The solvent volume was partially removed using a rotary evaporator. Finally, we cleaned the reaction

product by dialysis and centrifugation, obtaining a suspension with a concentration of 1.46% w/w measured by thermogravimetric analysis. This method makes PS/PNIPAM core–shell particles without anchoring PNIPAM onto the PS core. Since the cross-linking and growing process of the PNIPAM shell are driven just by the AIBN initiator, it was unnecessary to use another control agent. Therefore, our PS/PNIPAM particles are not significantly charged. The hydrodynamic radius of our PS/PNIPAM core–shell particles at 20 °C (swollen state) is 298.5 nm, and at 40 °C (shrunk state), the radius is 159.5 nm.

B. Light scattering

Hydrodynamic radius (R_h) was measured by dynamic light scattering (DLS), and the angular scattering intensity by static light scattering (SLS) using a multi-angle light scattering setup (LS Instruments AG, Switzerland) with $\lambda = 632.8$ nm in a vertical–vertical polarization configuration. In addition, 0.005% w/w particle suspensions were placed in NMR glass tubes (Diam. 5 mm) for DLS and SLS measurements. The DLS measurements were made at scattering angles from 60° to 120° with a step of 5° for 60 s; the results were analyzed by cumulants to obtain the mean R_h of particles. The SLS measurements were made at a scattering angle from 30° to 135° with a step of 1°, taking 50 measurements of 1 s for each angle. The SLS average results for our suspension, $I_s(\theta)$, were analyzed considering the toluene and the water scattering line, $I_{Tol}(\theta)$ and $I_w(\theta)$, using the following formula: $I(\theta) = (n_w/n_{Tol})^2 R_{Tol}(I_s(\theta) - I_w(\theta))/I_{Tol}(\theta)$, where $n_w = 1.332$ and $n_{Tol} = 1.494$ are water and toluene refractive indices, respectively; $R_{Tol} = 1.020\,74 \times 10^{-5}$ cm^{-1} is the toluene Rayleigh ratio.

C. Numerical method

To assess the Mie scattering model using the multilayer sphere approximation to describe the PNIPAM light scattering intensities, we fit them to the experimental scattering intensity data as a function of the scattering angle using the least-squared minimization. Our numerical method needs eight parameters: λ, n_0, R_h, R_c, n_c, σ_{gc}, R_s, and σ_{gs}. Here, σ_{gc} and σ_{gs} are the geometric standard deviations of the core and shell radius, respectively. However, n_0, R_h, and λ are fixed parameters defined by the scattering experiment.

The numerical method makes the following steps: (a) Reading input experimental variables: λ, n_0, R_h, and other variables depending on the known parameters of the system under study, namely, R_c and n_c; variables used for the fitting as the number of layers to make up the multilayer sphere, L, are described in Sec. II A. The number L of layers dictates how the RI profile is discretized. So, we considered two criteria for choosing L. (i) The accuracy between the scattering intensity curves generated by RI profiles discretized with a large L number of layers (as many layers as the discrete RI profile and the continuous RI profile are essentially indistinguishable) and that discretized with few layers. (ii) The use of a practical computing time, which is a function of L. In the supplementary material, we discuss the details of the dependence of the scattering form factor curves on L. (b) Reading the experimental intensity data, which consists of a table with three columns: angle in degrees, θ_i, intensity in arbitrary units (a.u.), $I(\theta_i)$, and the experimental standard error of $I(\theta_i)$, α_i. (c) Development of the fitting numerical scheme. In this procedure, we will calculate the scattering intensities denoted by $\hat{I}(\theta_i)$ for different sets of fitting parameters (circumflexed variables are calculated using fitting parameters). To that end, we calculate a form factor $\hat{F}(\theta_i)$ using the theoretical model described above for each angle θ_i. First, we calculate σ of Eq. (11) to make a table for the refractive index profile with L rows. Then, the scattering coefficients a_n and b_n of Eqs. (9) and (10) as well as the angular functions $\pi_n(\theta)$ and $\tau_n(\theta)$ of Eq. (4) are calculated, truncating the series index, n, using the Wiscombe criterion.[30,35,39] Finally, $\hat{F}(\theta_i)$ is calculated using Eqs. (1)–(3). The same procedure is used for each set of parameters for the polydisperse case; see Eq. (12). From here, the numerical fitting process described in Subsection III D ensues.

It is important to mention that the Mie scattering theory numerical method applied to a nonhomogeneous spherical colloid implemented in this work, excluding the way of approximating the particle inhomogeneity, corresponds to the exact solution for the scattered field as given by the electromagnetic theory that relates the incident electromagnetic wave on a scatterer particle with the scattered field as given in Ref. 35. In contrast, RGD is an approximation that applies for very weak scatterers, i.e., the presence of the particles does not alter the field and is identical to the incident wave. The particle must reflect very little ($|n_p/n_o - 1| \ll 1$), and it must introduce negligible phase shift $4\pi n_0 R|m-1|/\lambda \ll 1$; the refractive indexes' imaginary part is negligible in all the cases.[29] Despite the mathematical complexity of Mie scattering theory, our procedure is customizable for specific requirements depending on the available information about the scatterer particles. The whole numerical method used in this study can be found in a public repository (https://github.com/Complex-Fluids-IFUNAM/Mie-Scattering).

D. Fitting numerical scheme

We use the iterative grid search method, implemented through iterative nested loops, to minimize the Chi-square goodness of fit parameter, $\chi^2 = \sum_i (y_i - \hat{y}_i)^2/\alpha_i^2$, where y_i and $\hat{y}_i$ are the experimental and calculated data using the fitting parameters, respectively, and α_i is the uncertainty of the experimental data.[40] The minimum χ^2 will determine the best-fitting parameters. The grid search method may converge very slowly toward the minimum χ^2, so we must consider previously known system information, such as the hydrodynamic radius or PNIPAM's bulk refractive index, to set the most appropriate search intervals for the fitting parameters; otherwise, computing time increases considerably. We can reduce the computing time by considering a minimum χ^2 threshold or by increasing the search step on the fitting parameters. Our grid search procedure begins at the lower limit in an upward search along the R_c interval, and for all R_c, an upward iterative search starts along the R_s interval. For all R_c and R_s, a downward iterative search starts along n_c. For all R_c, R_s, and n_c combinations of this grid search, the form factor function for a monodisperse system and χ^2 are then calculated. If χ^2 is near an initial minimum threshold, $\chi^2_{\min}$, i.e., $\chi^2 \le \chi^2_{\min} + \delta$, we start an iterative upward search along the polydispersity parameters σ_{gc} and σ_{gs}. If $\chi^2 < \chi^2_{\min}$, then a new minimum threshold was found, and now $\chi^2_{\min} = \chi^2$. Always, we update $\chi^2_{\min}$ until no new smaller χ^2 is found. In any other case, the iterative process continues when the search along the n_c interval ends and then until the search along the R_s interval for all n_c values end, stopping the search when all the

values of the R_c interval ended. To avoid losing any set of parameters that minimizes χ^2, an arbitrary δ is selected that permits an efficient search. In our case, we select $\delta = 10\,\chi^2_{\min}$.

IV. RESULTS AND DISCUSSION

A. Predictions for the multilayer Mie approximation

To get some physical insight into how the different values of the involved parameters affect the features of the form factor, in the supplementary material, we describe the resulting form factors with the method described above for several core–shell particles with a non-constant RI profile, i.e., core–shell structures with an inner core of constant RI and a fuzzy shell, where the RI decays as a Gaussian function.

In the following discussion, we describe the calculation of form factors for more interesting core–shell particles, which have a refractive index distribution with spherical symmetry. However, n_c is varied to be similar to the surrounding liquid, or they have an additional RI plateau in the shell (a layer with a constant RI). These examples could be interesting models for describing microgels with super chaotropic agents bound to the microgel structure, hollow microgels, or microparticles. Figure 4(a) shows the form factors for core–shell particles with R_c = 100 nm and R_s = 450 nm, where the index of refraction of the core goes from n_c = 1.35, a value close to that of the outer fluid, n_o = 1.33, up to n_c = 1.60. However, the RI profile of the shell at the boundary with the core always starts at 1.45 (see the inset). It should be noted that the case of n_c = 1.35 corresponds to a hollow particle. Here, the scattering is relatively low, and the scattering intensity increases as the refraction index contrast between the core and the index as the shell boundary increases; however, the form factors present a low structure due to the small core size. Figure 4(b) is similar to Fig. 4(a), but we included an RI plateau of 1.45 on the shell, as shown in the inset. This situation is similar to what occurs with PNIPAM core–shell particles, where, in addition to the core, there is some kind of additional denser PNIPAM layer in the shell. The RI decays with a Gaussian profile after the PNIPAM RI plateau. In all the cases, the scattering significantly increases with the inclusion of this RI plateau in the shell.

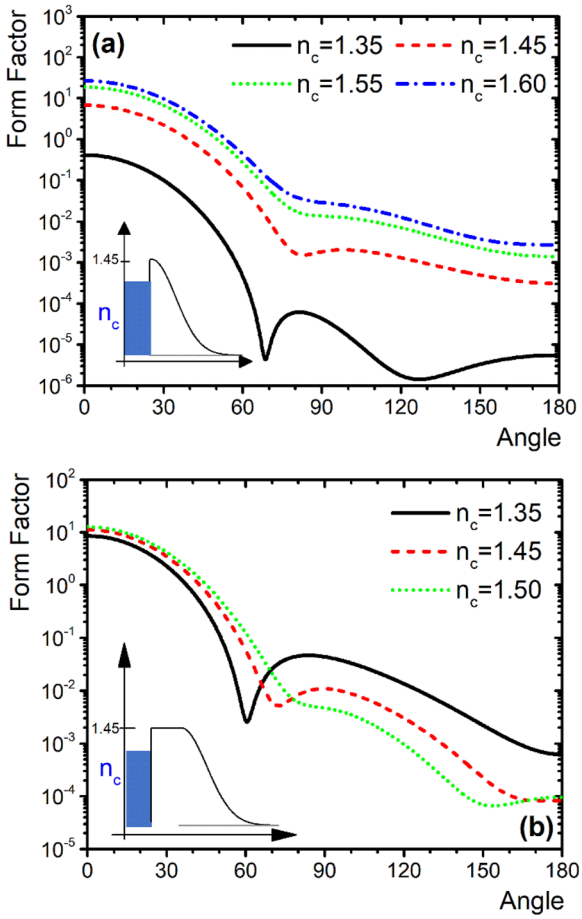

FIG. 4. (a) Form factors for core–shell particles in the cases where RI varies from low to large RI. However, the RI profile of the shell at the boundary with the core always starts at n_c = 1.45; R_c = 100 nm, R_s = 450 nm, n_o = 1.33, and λ = 632.8 nm. (b) The same as panel (a), but here, an RI plateau in the shell (RI = 1.45) is included. R_c = 100 nm, R_s = 450 nm, and the RI plateau in the shell = 50 nm, n_o = 1.33, and λ = 632.8 nm.

B. PNIPAM microgels

As mentioned earlier, some authors suggest that the PNIPAM RI profile is well modeled by Eq. (11). However, although it was tested by comparing it to actual refractive index measurements with good results,[16] this profile needs an assessment to give form factor functions for PNIPAM microgels. It is a common practice that the form factor function of PNIPAM microgels is obtained by fitting the fuzzy sphere model to the experimental SLS data.[15–17,27] Reufer *et al.*[17] studied PNIPAM microgel form factors using unpolarized SLS (λ = 680.4 nm) over a temperature range of 10 °C ≤ T ≤ 40 °C. Their PNIPAM microgels were synthesized by free radical cross-linking polymerization of NIPAM with N, N′-Methylene-BiS-Acrylamide (BIS) using potassium persulfate (KPS) as the polymerization initiator. They measured R_h, and their particles ranged from 468 nm at 10 °C (swollen state) to 271 nm at 40 °C (shrunk state). The sizes of their particles are typically in the Mie scattering regime. However, they used the RGD approximation to fit the experimental scattering intensities to obtain their parameters. Figure 5 shows their experimental scattering intensity vs scattering angle given for different temperatures. In this figure, we included the calculated scattering intensities using the method we proposed in Subsection III C and those of Reufer *et al.*[17] using the RGD approximation. The scattering intensity in a diluted suspension is proportional to the form factor because the structural information, given by the static structure function, is essentially one. We can observe in Fig. 5 that the RGD approximation fits the experimental data with an acceptable agreement for temperatures below LCST because the microgel is in a swollen state where its effective refractive index is sufficiently low to satisfy the RGD conditions. The RGD approximation fit reproduces the first form factor minimum. However, this does not occur for the second one at high scattering angles. For temperatures above LCST, the RGD approximation fit is far from the experimental scattering intensities because the microgel, in a shrunk state, is like a homogeneous sphere with a high refractive index. The authors estimated the maximum RI of their microgel as n_p = 1.46 at the maximum

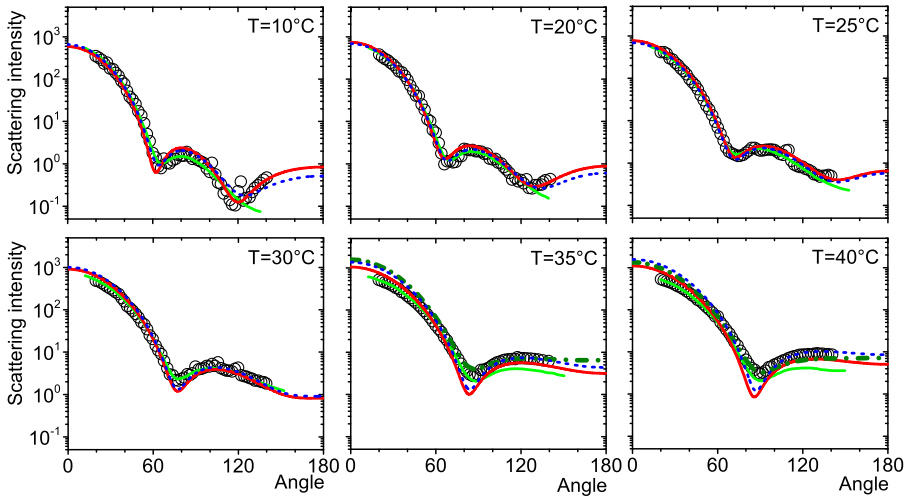

FIG. 5. Scattering intensity (arbitrary units) vs scattering angle (degrees). Experimental temperature-dependent scattering intensities as a function of scattering angle (circles, from Reufer *et al.*[17]). The best fit for MSA1 and MSA2 are represented by the solid red lines and blue dashed lines, respectively, up to 40 °C. At 35 and 40 °C, SSPH is indicated by the dark green dashed–dotted lines. RGD approximation fits with a polydispersity of 9.5% indicated by the solid green lines, according to the work by Reufer *et al.*[17]

collapsed state, whereas if the water RI $n_w = 1.332$, then the RGD conditions are not fully met ($|n_p/n_w - 1| \ll 1$). Reufer *et al.*[17] made their calculations considering a polydispersity of 9.5% in all cases. The parameters obtained from the fitting to their experimental data using the RGD approximation are presented in Table I.

Our results, also shown in Fig. 5, fit the same experimental data Reufer *et al.*[17] gave. To make these fits, we need for each case the proportional constant, κ, which involves the device's experimental details. Because we do not know κ, we run two different fitting routines to match our calculated form factors to the experimental data; we will name these routines as multilayer sphere approximations (MSAs). In the first MSA fit routine 1 (MSA1), we calculate κ as an average of the following ratios: $\kappa = 0.5\left[I(\theta_1)/\hat{F}(\theta_1) + I(\theta_N)/\hat{F}(\theta_N)\right]$, where the angles θ_1 and θ_N are the first and the last experimental points; $\hat{F}(\theta_i)$ and $I(\theta_i)$ are the calculated form factor with the parameters to be fit and the experimental intensities, respectively. In the second MSA fit routine 2 (MSA2), we calculate κ as the average for all experimental point ratios and calculated the form factor values, i.e., $\kappa = (1/N)\sum_{i=1}^{N}\left[I(\theta_i)/\hat{F}(\theta_i)\right]$. In both cases, the predicted scattering intensity for our model would be $\hat{I}(\theta_i) = \kappa\hat{F}(\theta_i)$. It is important to note that the MSA1 routine calculation is a relaxed version of the MSA2 routine, which we employed for noisy experimental data. Then, we minimized the goodness of the fit parameter, χ^2, to determine the best-fit parameters of our model in the two described versions, MSA1 or MSA2. We set the range of the core RI fit variable between 1.332 (water RI) and 1.46, which is the maximum RI expected at the collapsed state. For the core and shell radius fit variables, we set a maximum at the hydrodynamic radius reported by Reufer *et al.*[17] The polydispersity fit variables have only a non-overlapping condition to avoid values where $R_c \geq R_s$. In all cases, for the core and shell's radius, the searching steps are $\Delta R_c = \Delta R_s = 1.0$ nm, for the core's refractive index, $\Delta n_c = 0.01$, and for the core and shell's polydispersity parameter, the searching steps are

TABLE I. Parameters obtained using different approximations parameters for the best-fit values using MSA1 and MSA2, as well as the results by Reufer *et al.*[17] for a hydrodynamic radius R_h as a function of temperature T and their best-fit parameters using the RGD approximation. All the radius values are in nanometers, the temperature in °C, and κ in arbitrary units.

		RGD	MSA1						MSA2					
T	R_h	R	R_c	n_c	σ_c	R_s	σ_s	κ	R_c	n_c	σ_c	R_s	σ_s	κ
10	468	335	292	1.44	1.13	432	1.01	33.09	255	1.44	1.13	468	1.01	42.46
20	433	321	257	1.46	1.13	433	1.00	42.10	242	1.45	1.15	440	1.00	51.29
25	416	308	229	1.46	1.15	415	1.00	69.02	229	1.46	1.15	416	1.00	61.39
30	383	290	242	1.46	1.09	349	1.00	118.04	242	1.46	1.09	349	1.00	131.5
35	299	262	243	1.46	1.05	299	1.00	203.42	242	1.46	1.05	298	1.00	270.6
40	271	257	249	1.46	1.02	271	1.00	623.35	246	146	1.02	268	1.00	380.5

$\Delta\sigma_c = \Delta\sigma_s = 0.01$. In all the cases, the total computing times employed in the fit routines are presented in Tables SMX1 and SMX2 in the supplementary material. The parameters obtained from fitting the experimental data using MSA1 and MSA2 are presented in Table I. Figure 5 shows the results for both MSA1 fit and MSA2 fit from 10 to 40 °C. MSA1 and MSA2 present an excellent agreement up to 30 °C. MSA1 at 10 and 20 °C slightly shifts the first form factor minimum to small angles, whereas MSA2 replicates the first form factor minimum very well but not the second minimum. This may be due to a deficient weighted error evaluation of the experimental points at high scattering angles with smaller intensity values. MSA1 and MSA2 produce better fits than RGD approximation because RGD cannot replicate the second form factor minimum. MSA1 and MSA2 fit at 25 °C are very similar and give a better description of the experimental data than RGD approximation. At 30 °C, MSA1, MSA2, and RGD approximation fits are practically the same. Reufer *et al.*[17] mentioned that this is a limit case because even a single sphere fit can describe the experimental data well but underestimate the microgel radius. On the other hand, at 35 and 40 °C, the multilayered sphere fails as expected because the microgel in a shrinking state is like a solid homogeneous sphere. The PNIPAM microgel cannot be described as a core–shell sphere with a fuzzy shell above LCST. The Mie scattering theory for a homogenous sphere is the best model that describes this microgel's scattering behavior, although it presents deviations from the experimental data, as shown in Fig. 5.[14,17] We use Bohren and Huffman's single homogeneous SPHere algorithm (SSPH) to make these fittings.[35]

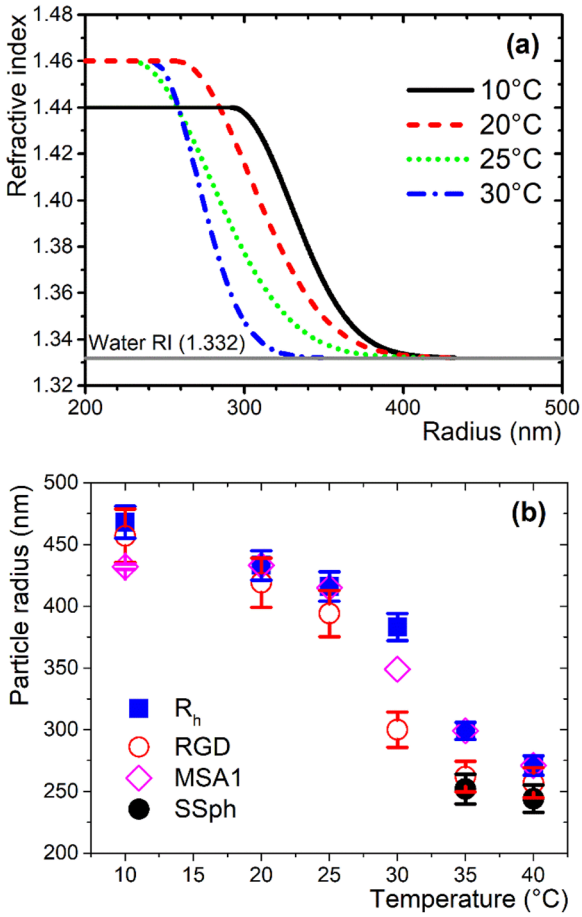

FIG. 6. (a) Radial refractive index profile of MSA1 fitted for the microgel in the swollen state. (b) Comparison of particle hydrodynamics radius (experimental ■) as a function of the temperature with our model predictions. We included the RGD fits from the work by Reufer *et al.*[17] and the particle radius from the solid sphere model at 35 and 40 °C.

Figure 6(a) shows the radial RI profiles from the MSA1 fits on Table I, and Fig. 6(b) shows a comparative graph for measured and fitted particle radius using different theoretical methods. The RI fit values of the microgel core at 10 °C give $n_c = 1.44$ and for temperatures >10 °C, an almost constant value, which is $n_c = 1.46$. This last value also coincides with the maximum estimated RI given by Reufer *et al.*[17] This could reveal that the core of the PNIPAM microgel contains the same amount of water in the swollen state when the suspension is close to the LCST. Figure 6(b) shows that MSA1 slightly underestimates particle radius at 10 and 30 °C. At other temperatures, the MSA1 fits agree with the hydrodynamic radius measured by Reufer *et al.*, even at microgeles in the shrunk state. There is an important observation shown in Fig. 6(b), despite the RGD fit presents an excellent agreement at 30 °C, it leads to an error in evaluating the microgels' expanded to shrunk transition temperature (~32 °C) with a percentage deviation of 21.7% from R_h, whereas for the MSA1 fitted radius at 30 °C, the percentage deviation is 8.9% from R_h. On the other hand, at 35 and 40 °C, SSPH underestimates the hydrodynamic particle radius despite its better description than the Gaussian RI profile model. This fact could reveal that the radial refractive index profile in the collapsed state is more complex than homogeneous or Gaussian profiles. As far as we know, this is the first time that the form factor of PNIPAM microgel in the swollen state is described in the Mie scattering regime using a radial refractive index profile.

C. PS/PNIPAM core shell particles

Figure 7(a) shows our experimental scattering intensities vs scattering angles for PS plain standard particles with mean diameter = 100 nm (Bangs Laboratories, Inc. USA) (black squares), showing that the calibration of our SLS device is correct, and PS/PNIPAM core–shell particles at 20 °C (red circles) and 40 °C (blue triangles) synthesized by us. At small scattering angles, we can observe that PS/PNIPAM core–shell particles scatter around one order of magnitude more than PS plain standard particles, even though PS plain standard particles and the core of PS/PNIPAM particles have a very close size. To fit the experimental scattering data shown in Fig. 7(a), we use a similar procedure to MSA2 because it presents a low experimental noise. This allows us to estimate κ rigorously without any data masking. Considering that scattering intensities are measured in vertical polarization setup, the proportionally constant κ is calculated as an average of all the experimental point ratios with $|\hat{S}_1(\theta)|^2$, i.e., $\kappa = (1/N)\sum_{i=1}^{N}\left[I(\theta_i)/|\hat{S}_1(\theta_i)|^2\right]$, where the scattering amplitude, $|\hat{S}_1(\theta)|^2$, is given in Eq. (2) and is calculated with single sphere Mie or multilayer sphere Mie approximation, as appropriate. Therefore,

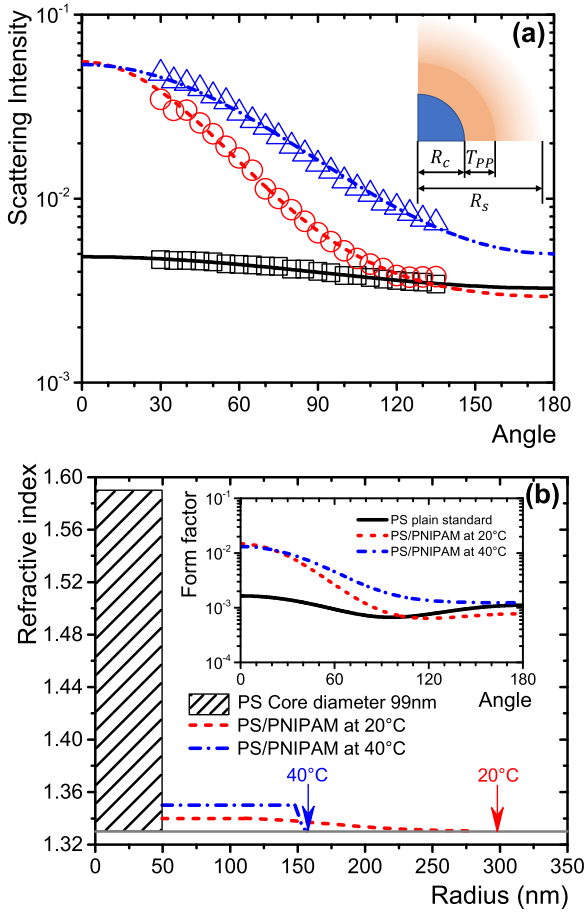

FIG. 7. (a) Experimental temperature-dependent scattering intensity (arbitrary units) as a function of the scattering angle (degrees) of PS plain standard particles with 100 nm of mean diameter (black squares) and of PS/PNIPAM at 20 °C (red circles) and 40 °C (blue triangles). Models: single sphere for PS plain standard particles (black line); MSA2 for core–shell particles are indicated by the red dashed and blue dashed–dotted lines at 20 and 40 °C, respectively. The inset presents a cartoon of the core–shell particle structure. Panel (b) presents the RI profiles from fits to the experimental data of PS/PNIPAM particles at 20 and 40 °C; the dashed rectangle represents the PS core. The inset presents the form factor fits for the PS plain and core–shell particles.

in both cases, the predicted scattering intensity for our model would be $\hat{I}(\theta_i) = \kappa|\hat{S}_1(\theta_i)|^2$, and we will name these routines SSPH and MSA3, respectively. We considered that the PS/PNIPAM particles have a monodisperse PS core with homogeneous RI, $n_{PSC} = 1.59$. We take as the nominal size of PS cores, R_{PSC}, those reported by the manufacturer, $R_{PSC} = 49.5$ nm. We approximate the RI of the PNIPAM shell as a Gaussian RI profile given by Eq. (11). Therefore, in the multilayered sphere approximation, the parameters obtained from the best fit are the thickness and RI of the PNIPAM RI plateau in the shell, T_{PP} and n_{PP}, respectively, as well as the shell radius, R_s, and the polydispersity of the PNIPAM RI plateau in the shell, σ_{PS}, and shell σ_S [see the inset in Fig. 7(a)].

TABLE II. Parameters for the MSA3 best fit from the experimental data of our PS/PNIPAM particles at 20 and 40 °C and the hydrodynamic radius measured by DLS. The radius and thickness values are in nanometers, the temperature is in °C, and κ is in arbitrary units.

		MSA3					
T	R_h	T_{PP}	n_{PP}	σ_{PP}	R_s	σ_S	κ
20	298	42.5	1.34	1.15	298	1.14	3.80
40	159.5	92.5	1.36	1.00	144	1.00	2.88

To fit the experimental data of PS plain standard particles, we used the SSPH routine. We set the hydrodynamics radius provided by DLS as an upper search limit value for the particle radius. For PS/PNIPAM particles, to save computing time, we first fit the PS/PNIPAM experimental data for 40 °C, whose results allow us to set the search limits for PS/PNIPAM at 20 °C because at 40 °C, the PNIPAM shell is shrunk, and a large amount of water is expelled. Hence, at 40 °C, the PNIPAM RI plateau must be at maximum, setting an upper search limit value for the PNIPAM RI plateau for 20 °C. Then, we first fit the data corresponding to 40 °C, setting the range of the PNIPAM RI plateau between the water RI and 1.46, where 1.46 is the RI plateau value fitted for the PNIPAM microgels (see Sec. III A 2). The thickness search range is set between the core and hydrodynamic radius. The upper search limit for the particle radius at 20 and 40 °C is the hydrodynamics radius provided by DLS (see Table II). To end this fit, we determine the PS/PNIPAM search ranges at 20 °C. We set the same search steps for the size, refractive index, and polydispersity parameters used in the MSA1 and MSA2 routines. The total computing time employed in the fit routines is presented in Table SMX3 in the supplementary material.

The best-fit value for the PS standard plain particles is $R = 51.3$ nm with a monodisperse distribution. The best-fit values for PS/PNIPAM particles are presented in Table II. In all cases, the scattering intensities fitted agree well with the experimental data, and these results could show that the shell grew with a uniform size in our PS/PNIPAM synthesis, and the structural differences of the shell due to the synthesis process can be observed below LCST, where the size of PNIPAM RI plateau in the shell and the size of the shell are not monodisperse. The best-fit parameter of MSA3 for our PS/PNIPAM particles at 20 and 40 °C is presented in Table II.

Figure 7(b) shows the radial RI profile for the MSA3 calculation obtained by the best fit to the experimental data. Here, we can observe that the coating is not very dense, but despite this, the scattering properties of the PS/PNIPAM particles are dominated by the optical and geometrical parameters of the shell. In the inset of Fig. 7(b), we show the form factor function, calculated using Eq. (1), corresponding to the best-fit scattering intensity of Fig. 7(a). The PS plain standard particles scatter in the Rayleigh scattering regime due to its small size.[35] As we observe from our calculations, the shell is responsible for losing the Rayleigh scattering behavior. As far as we know, our results are the first attempt to describe the form factor and the RI profile of this kind of composite particle in the Mie scattering regime.

Before ending this section, we would like to mention that we tried to describe core–shell particle suspensions with a PS

spherical core coated with PNIPAM cross-linked with acrylic acid (PS/PNIPAM-co-AAc)[18] using a PS core with homogeneous RI, a PNIPAM plateau, and a Gaussian RI decay as a refractive index profile model. The fitted scattering intensities vs angle agree pretty well with the experimental data [Fig. SM4(a) in the supplementary material]. However, the radial RI profiles obtained from the fitted scattering intensities at 25 and 35 °C produced the best-calculated shell radii that significantly underestimated the experimental hydrodynamic measured radius [Fig. SM4(a) in the supplementary material]. Therefore, the RI profile of the PNIPAM-co-AAc is probably not well described by the proposed model for $n(r)$, and several profiles must produce the same experimental scattering intensities.

V. CONCLUSION

This work presented how to apply Mie scattering theory to predict and understand the static light scattering of large nonhomogeneous colloidal particles of a size comparable with the light wavelength used for developing light scattering experiments. The colloidal particles used in this study form scatterers with a constant refractive index core and a shell with a refractive index decaying until it matches the solvent refractive index, forming a core–shell structure, which was approximated by a Gaussian RI profile numerically evaluated through a multilayer sphere. We calculated the form factor functions of suspensions of PNIPAM and PS/PNIPAM. For the PNIPAM case presented in Ref. 17, the scattering intensity is very well predicted in the swollen state, as shown by their excellent fit with the experimental scattering intensities. In the shrunk state, the Gaussian RI profile cannot describe the radiative properties as expected because the microgel is like a solid homogeneous sphere; we must use the standard Mie scattering theory. As far as we know, this is the first time that the form factor of PNIPAM microgel in the swollen state is described in the Mie scattering regime using a radial refractive index profile. We also successfully described the light intensity form factors of PS/PNIPAM microgel particles synthesized by us. In the future, our next step would be to study more core–shell systems to determine the limits of the model and to improve the computational algorithms used for these calculations, as to introduce a numerical procedure for selecting L intelligently considering independent criteria of the particle's size and refractive index profile to use less computing time, and to implement numerical routines to calculate the uncertainties of calculated physical quantities and more efficient methods for χ^2 minimization.

Mie scattering theory is an improvement of RGD. As mentioned in Subsection III C, RGD has to be used for small scatterers, compared to the wavelength of the incident laser radiation, with a slight refractive index difference from the surrounding solvent. Mie scattering theory corresponds to the exact solution for the scattered field, as given by the electromagnetic theory, which relates the incident electromagnetic wave on a scatterer particle to the scattered field. Although mathematically involved, the computational algorithm we developed can be found in a public repository and can be freely used.

Our results could help in the study of microgels with large particles, as in the case of super chaotropic agents bound on the microgel structure,[10] or hollow microgel particles,[5,34] and also in developing numerical tools for light scattering for core–shell particles with a fuzzy shell to design optical switches.[18] In addition, knowing the light scattering of suspensions made of mesoscopic core–shell particles makes it possible to predict their photonic properties as the transport mean-free path of light,[17,41] more experimental data in this direction are being developed by us with suspensions of PS/PNIPAM core–shell particles of different sizes, concentrations, and temperatures, where SLS data and transport mean-free path of light in these suspensions are evaluated and compared to experiments; these results would be presented shortly. Our Mie scattering multilayer model could be extended to better understand the radiative properties of fuzzy materials' core–shell particles with a metallic core. Since our method can include imaginary refractive indices, it could be an alternative to the RGD approximation and Monte Carlo simulations to describe the absorption spectra of core–shell gold particles coated with PNIPAM as made by Ponomareva *et al.*[27,33] On the other hand, since the extinction cross section is related to the scattered light and, consequently, to the amplitude scattering coefficients, the Mie scattering can be related to light extinction spectroscopy, which looks for a nonintrusive characterization of submicron particles. The influence of the internal structure of inhomogeneous particles on their radiative properties is an open issue in many fields of science and technology.[42,43] Our model for multilayered spheres could be a starting point for studying particles with spherical symmetry. Furthermore, video holographic microscopy characterization of colloidal spheres has been developed by a fit of their measured hologram normalized images to a theoretical expression of these normalized images, which involves the Mie scattering coefficients where its radius and its refractive index are used as free parameters.[44] A natural extension of this experimental technique could be using the Mie scattering model for multilayered spheres to characterize more complex colloidal particles.

SUPPLEMENTARY MATERIAL

The supplementary material encompasses discussion on predictions of the form factor for core–shell structures; dependence of scattering form factor curves on L; computing time tables of MSA1, MSA2, and MSA3 routines, and on PS/PNIPAM-co-AAc core–shell particles.

ACKNOWLEDGMENTS

We thank C. Garza for their technical support. We thank Dr. Pedro Diaz-Leyva from UAM-I for the help and facilities to develop our LS experiments and from Fis. A. Ovando-Avalos for his help in some numerical calculations.

We acknowledge the financial support from SEP CONAHCYT (A1-S-15587), DGAPAUNAM (IN 104024), and the CONAHCYT scholarship for CB-C.

AUTHOR DECLARATIONS

Conflict of Interest

The authors have no conflicts to disclose.

Author Contributions

Christian Balderas-Cabrera: Conceptualization (equal); Funding acquisition (equal); Investigation (equal); Software (equal); Supervision (equal); Writing – review & editing (equal). **Rolando Castillo**: Conceptualization (equal); Funding acquisition (equal); Investigation (equal); Software (equal); Supervision (equal); Writing – review & editing (equal).

DATA AVAILABILITY

The Mie Scattering multilayer model numerical methods used in this study can be found in the numerical methods presented in a public repository (https://github.com/Complex-Fluids-IFUNAM/Mie-Scattering) after the publication of this paper.

REFERENCES

[1]T. Okano, A. Kikuchi, Y. Sakurai, Y. Takei, and N. Ogata, "Temperature-responsive poly(*N*-isopropylacrylamide) as a modulator for alteration of hydrophilic/hydrophobic surface properties to control activation/inactivation of platelets," J. Controlled Release **36**, 125–133 (1995).

[2]T. M. Allen and P. R. Cullis, "Drug delivery systems: Entering the mainstream," Science **303**, 1818–1822 (2004).

[3]M. Motornov, Y. Roiter, I. Tokarev, and S. Minko, "Stimuli-responsive nanoparticles, nanogels and capsules for integrated multifunctional intelligent systems," Prog. Polym. Sci. **35**, 174–211 (2010).

[4]J. Huang, M. Li, and D. Fan, "Core-shell particles for devising high-performance full-day radiative cooling paint," Appl. Mater. Today **25**, 101209 (2021).

[5]J. Oberdisse and T. Hellweg, "Recent advances in stimuli-responsive core-shell microgel particles: Synthesis, characterisation, and applications," Colloid Polym. Sci. **298**, 921–935 (2020).

[6]B. Groever, B. Heshmat, and R. Raskar, "Tyndall windows: Tunable scattering of disordered solid–liquid matching mixtures," ACS Photonics **3**, 930–935 (2016).

[7]M. Wu, Y. Shi, R. Li, and P. Wang, "Spectrally selective smart window with high near-infrared light shielding and controllable visible light transmittance," ACS Appl. Mater. Interfaces **10**, 39819–39827 (2018).

[8]Y. Shymborska, A. Budkowski, J. Raczkowska, V. Donchak, Y. Melnyk, V. Vasiichuk, and Y. Stetsyshyn, "Switching it up: The promise of stimuli-responsive polymer systems in biomedical science," Chem. Rec. **24**, 202300217–202300218 (2024).

[9]A. Eklund, S. Hu, Y. Fang, H. Savolainen, H. Pi, H. Zeng, A. Priimagi, O. Ikkala, and H. Zhang, "Bright and switchable whiteness in macro-crosslinked hydrogels," Adv. Opt. Mater. **12**, 2302487 (2023).

[10]J. Simons, N. Hazra, A. V. Petrunin, J. J. Crassous, W. Richtering, and M. Hohenschutz, "Nonionic microgels adapt to ionic guest molecules: Superchaotropic nanoions," ACS Nano **18**, 7546–7557 (2024).

[11]R. Pelton, "Temperature-sensitive aqueous microgels," Adv. Colloid Interface Sci. **85**, 1–33 (2000).

[12]B. W. Garner, T. Cai, S. Ghosh, Z. Hu, and A. Neogi, "Refractive index change due to volume-phase transition in polyacrylamide gel nanospheres for optoelectronics and bio-photonics," Appl. Phys. Express **2**, 057001 (2009).

[13]A. Halperin, M. Kröger, and F. M. Winnik, "Poly(*N*-isopropylacrylamide) phase diagrams: Fifty years of research," Angew. Chem., Int. Ed. **54**, 15342–15367 (2015).

[14]F. Scheffold, "Pathways and challenges towards a complete characterization of microgels," Nat. Commun. **11**(1), 4315 (2020).

[15]M. Stieger, W. Richtering, J. S. Pedersen, and P. Lindner, "Small-angle neutron scattering study of structural changes in temperature sensitive microgel colloids," J. Chem. Phys. **120**, 6197–6206 (2004).

[16]M. Ledesma-Motolinía, M. Braibanti, L. F. Rojas-Ochoa, and C. Haro-Pérez, "Interplay between internal structure and optical properties of thermosensitive nanogels," Colloids Surf., A **482**, 724–727 (2015).

[17]M. Reufer, P. Díaz-Leyva, I. Lynch, and F. Scheffold, "Temperature-sensitive poly(N-Isopropyl-Acrylamide) microgel particles: A light scattering study," Eur. Phys. J. E **28**, 165–171 (2009).

[18]G. Meng, V. N. Manoharan, and A. Perro, "Core-shell colloidal particles with dynamically tunable scattering properties," Soft Matter **13**, 6293–6296 (2017).

[19]D. S. Wiersma, "Disordered photonics," Nat. Photonics **7**, 188–196 (2013).

[20]C. Wei, X. Lu, X. Wen, Y. Liu, and S. Yang, "Thermo-responsive color-changeable photonic materials: A review," Opt Laser. Technol. **152**, 108135 (2022).

[21]T. Hellweg, "Responsive core–shell microgels: Synthesis, characterization, and possible applications," J. Polym. Sci., Part B: Polym. Phys. **51**, 1073–1083 (2013).

[22]X. Xu, Y. Liu, W. Fu, M. Yao, Z. Ding, J. Xuan, D. Li, S. Wang, Y. Xia, and M. Cao, "Poly(N-isopropylacrylamide)-based thermoresponsive composite hydrogels for biomedical applications," Polymers **12**, 580 (2020).

[23]T. R. Christiani, K. Toomer, J. Sheehan, A. Nitzl, A. Branda, E. England, P. Graney, C. Iftode, and A. J. Vernengo, "Synthesis of thermogelling poly(N-isopropylacrylamide)-graft-chondroitin sulfate composites with alginate microparticles for tissue engineering," J. Vis. Exp. **116**, e53704 (2016).

[24]J. H. Cho, R. Cerbino, and I. Bischofberger, "Emergence of multiscale dynamics in colloidal gels," Phys. Rev. Lett. **124**, 088005 (2020).

[25]L. Frenzel, F. Lehmkühler, M. Koof, I. Lokteva, and G. Grübel, "The phase diagram of colloidal silica-PNIPAm core–shell nanogels," Soft Matter **16**, 466–475 (2020).

[26]A. Dorodnyy, J. Smajic, and J. Leuthold, "Mie scattering for photonic devices," Laser Photonics Rev. **17**, 2300055 (2023).

[27]E. Ponomareva, B. Tadgell, M. Hildebrandt, M. Krüsmann, S. Prévost, P. Mulvaney, and M. Karg, "The fuzzy sphere morphology is responsible for the increase in light scattering during the shrinkage of thermoresponsive microgels," Soft Matter **18**, 807–825 (2022).

[28]O. L. J. Virtanen, A. Mourran, P. T. Pinard, and W. Richtering, "Persulfate initiated ultra-low cross-linked poly(*N*-isopropylacrylamide) microgels possess an unusual inverted cross-linking structure," Soft Matter **12**, 3919–3928 (2016).

[29]O. Glatter, in *Neutrons, X-Rays and Light: Scattering Methods Applied to Soft Condensed Matter*, *North Holland Delta Series*, edited by P. Lindner and T. Zemb (Elsevier Science, Amsterdam, 2002).

[30]W. Yang, "Improved recursive algorithm for light scattering by a multilayered sphere," Appl. Opt. **42**, 1710 (2003).

[31]B. R. Johnson, "Light scattering by a multilayer sphere," Appl. Opt. **35**, 3286 (1996).

[32]M. Kerker, *The Scattering of Light and Other Electromagnetic Radiation* (Elsevier, 1969).

[33]B. Tadgell, E. Ponomareva, M. Karg, and P. Mulvaney, "Scattering of visible light by Au–PNIPAM core–shell microgels," J. Phys. Chem. C **126**, 15336 (2026).

[34]D. Zhu, F. Wang, C. Gao, and Z. Xu, "Construction of PS/PNIPAM core-shell particles and hollow spheres by using hydrophobic interaction and thermosensitive phase separation," Front. Chem. Eng. China **2**, 253–256 (2008).

[35]C. F. Bohren and D. R. Huffman, *Absorption and Scattering of Light by Small Particles* (Wiley, Weinheim, Germany, 1998).

[36]A. L. Aden and M. Kerker, "Scattering of electromagnetic waves from two concentric spheres," J. Appl. Phys. **22**, 1242–1246 (1951).

[37]A. Quirantes, R. Plaza, and A. Delgado, "Static light scattering study of size parameters in core–shell colloidal systems," J. Colloid Interface Sci. **189**, 236–241 (1997).

[38]G. J. Ojeda-Mendoza, H. Contreras-Tello, and L. F. Rojas-Ochoa, "Refractive index matching of large polydisperse silica spheres in aqueous suspensions," Colloids Surf., A **538**, 320–326 (2018).

[39]W. J. Wiscombe, "Improved Mie scattering algorithms," Appl. Opt. **19**(9), 1505–1509 (1980).

[40]I. Hugues and T. Hase, *Measurements and Their Uncertainties* (Oxford University Press, 2010).

[41] L. F. Rojas-Ochoa, J. M. Mendez-Alcaraz, J. J. Sáenz, P. Schurtenberger, and F. Scheffold, "Photonic properties of strongly correlated colloidal liquids," Phys. Rev. Lett. **93**, 073903 (2004).
[42] I. T. Horvath, P. Colinet, and M. R. Vetrano, "Assessment of the light extinction spectroscopy technique for submicron particle characterization," Powder Technol. **291**, 375–382 (2016).
[43] R. E. H. Miles, A. E. Carruthers, and J. P. Reid, "Novel optical techniques for measurements of light extinction, scattering and absorption by single aerosol particles," Laser Photonics Rev. **5**, 534–552 (2011).
[44] S.-H. Lee, Y. Roichman, G.-R. Yi, S.-H. Kim, S.-M. Yang, A. v. Blaaderen, P. v. Oostrum, and D. G. Grier, "Characterizing and tracking single colloidal particles with video holographic microscopy," Opt. Express **15**, 18275 (2007).